International Journal of Thin Films Science and Technology

http://dx.doi.org/10.18576/ijtfst/150207

Collisionality-Controlled Transport of Sputtered Atoms in Argon: A Reproducible Monte Carlo Study Across Six Target Materials

Abdelkader Bouazza

L2GEGI Laboratory, University of Tiaret, 14000 Tiaret, Algeria

Received: 13 Mar. 2026, Revised: 2 Apr. 2026, Accepted: 26 Apr. 2026
Published online: 1 May 2026

Abstract: Gas-phase transport between a sputtering target and a substrate determines how much of the nascent flux survives, how strongly it thermalizes and with what angular distribution it arrives. In this work, a reproducible Monte Carlo campaign is used to quantify these coupled effects for Cu, Al, Ag, Ge, Si and Te sputtered into Ar at 300 K. The baseline design covers four pressures (0.3, 0.5, 0.8 and 1.0 Pa), four target–substrate distances (8, 12, 16 and 20 cm) and 20,000 launched particles per condition, giving 1.92 million trajectories. Initial energies are drawn from a truncated Sigmund–Thompson distribution, emission directions follow a cosine law, and emission points are distributed uniformly over the target area. Free flights are sampled from an energy-dependent effective transport cross section, and collisions are treated with elastic two-body hard-sphere kinematics. The computed observables are substrate transmission, collision counts, arrival-energy percentiles, high-energy fractions, radial spreading and incident angle. The median arrival energy decreases monotonically with both pressure and distance for all six materials, whereas the arithmetic mean can remain strongly influenced by a sparse energetic tail. Over the investigated window, $P{\cdot}L$ is a useful empirical collisionality coordinate, with median-energy regression R^2 values of 0.792–0.867 and material-specific slopes from -13.75 to -29.22 eV/(Pa m). Independent three-seed calculations and a 486-case sensitivity campaign show that the qualitative transport trends are robust, whereas absolute values depend on the adopted effective cross-section parameters. The framework therefore offers a transparent and reproducible basis for comparing species-dependent thermalization and transmission; it characterizes the arriving flux and is not intended as a direct predictor of film morphology or thickness.

Keywords: magnetron sputtering; Monte Carlo simulation; sputtered-atom transport; thermalization; collisionality; Sigmund–Thompson distribution; binary collisions

1 Introduction

During magnetron sputtering, atoms leave the target with a broad distribution of energies and directions and then undergo a stochastic sequence of free flights and collisions before reaching the substrate. Transport therefore controls quantities that can be computed directly, such as transmitted flux, collision number, arrival energy and incident direction, even though these quantities do not by themselves constitute predictions of film thickness, morphology or crystallographic texture. Monte Carlo transport modelling is well established for this problem, and more detailed approaches employ screened interaction potentials or coupled MC–MD treatments to resolve post-collision states [1–8].

The author and co-workers have previously examined the influence of pressure, temperature, geometry and the energy and angular distributions of sputtered particles using Monte Carlo approaches [9–15]. The present study builds on that work with a narrower and testable objective: to determine whether pressure and target–substrate distance can be organized through a common empirical collisionality coordinate, and to quantify how this response differs among six sputtered species within a fully reproducible computational campaign.

The study contributes four elements: (i) a fully specified stochastic source and transport model; (ii) a 96-condition baseline dataset containing 1.92 million trajectories; (iii) observables extending beyond mean energy to transmission, collision statistics, energy

* Corresponding author e-mail: abdelkader.bouazza@univ-tiaret.dz

percentiles, angular broadening and radial spreading; and (iv) explicit robustness tests using independent random seeds and systematic variation of the effective collision cross section [2,6,10,12,15].

2 Monte Carlo model

2.1 Source energy and kinematic upper bound

For a sputtered species of mass m_s interacting with argon of mass m_{Ar}, the maximum transferable energy scale is written as

$$E_{\max} = \gamma E_{\mathrm{ion}}, \qquad \gamma = \frac{4 m_{\mathrm{Ar}} m_s}{(m_{\mathrm{Ar}} + m_s)^2}. \tag{1}$$

The baseline ion energy is $E_{\mathrm{ion}} = 262$ eV. The initial sputtered-atom energy is sampled from the truncated Sigmund–Thompson distribution [1,6]

$$f(E) = \frac{C E}{(E + U_{\mathrm{b}})^3}, \qquad 0 < E < E_{\max}, \tag{2}$$

where C is a normalization constant and U_{b} is the effective surface binding-energy parameter assigned to the sputtered species. With the substitution $x = E/(E + U_{\mathrm{b}})$, the cumulative distribution becomes proportional to x^2, which gives an exact inverse-transform sampler:

$$x_{\max} = \frac{E_{\max}}{E_{\max} + U_{\mathrm{b}}}, \qquad x = x_{\max}\sqrt{R}, \qquad E = \frac{U_{\mathrm{b}} x}{1 - x}, \tag{3}$$

where R denotes a random number uniformly distributed on $(0, 1]$, drawn independently each time it appears.

2.2 Initial position and angular distribution

Emission positions are sampled uniformly over the circular target area. For a target radius $R_t = 2.5$ cm, the radial coordinate is sampled as

$$\rho = R_t \sqrt{R}. \tag{4}$$

The polar angle follows a cosine emission law over the upper hemisphere:

$$p(\theta) = 2 \sin\theta \cos\theta, \qquad \theta = \sin^{-1}\sqrt{R}, \tag{5}$$

with $0 \le \theta \le \pi/2$. The azimuthal angle φ is sampled uniformly over $0 \le \varphi < 2\pi$. These source assumptions are consistent with the simplified Monte Carlo representation adopted for reproducible transport comparisons; more detailed source correlations can be introduced in future work [1,2,6].

2.3 Gas density, free flights and collisions

The argon number density is obtained from the ideal-gas relation

$$n_{\mathrm{Ar}} = \frac{P}{k_B T_g}, \tag{6}$$

with $T_g = 300$ K. An energy-dependent effective transport cross section is used to make the collision frequency explicit:

$$\sigma(E) = \sigma_0 \left(\frac{E}{E_{\mathrm{ref}}} \right)^{-\alpha}, \tag{7}$$

where $E_{\mathrm{ref}} = 10$ eV, $\sigma_0 = 1.0 \times 10^{-19}$ m^2 and $\alpha = 0.18$. In the numerical implementation, $\sigma(E)$ is bounded between $0.3\sigma_0$ and $3\sigma_0$. The corresponding mean free path and stochastic free-flight distance are

$$\lambda(E) = \frac{1}{n_{\mathrm{Ar}}\,\sigma(E)}, \qquad s = -\lambda(E) \ln R. \tag{8}$$

At each collision, the impact parameter is sampled uniformly over the hard-sphere collision disk. The relative velocity is specularly reflected in the centre-of-mass frame, after which the projectile velocity is transformed back to the laboratory frame. This gives exact two-body elastic hard-sphere kinematics for the adopted collision model. The effective cross section is a modelling assumption; consequently, absolute transport values should be interpreted together with the sensitivity campaign described in Section 4.2 [2,5–8].

2.4 Geometry and simulation matrix

The baseline geometry contains a 5 cm-diameter circular target and a 40 cm-diameter circular substrate. Four pressures (0.3, 0.5, 0.8 and 1.0 Pa) and four target–substrate distances (8, 12, 16 and 20 cm) are combined for Cu, Al, Ag, Ge, Si and Te. Each of the 96 conditions uses 20,000 launched trajectories under a fixed seed policy, yielding 1,920,000 baseline trajectories. The matrix is designed to resolve coupled pressure–distance effects rather than to reproduce a single experimental apparatus [2–4,9–12,15].

2.5 Computed observables

For each condition, the program stores the initial energy, arrival energy, radial arrival coordinate, incident angle, collision count and arrival flag. The primary transmission metric and its binomial standard error are

$$T = \frac{N_{\mathrm{arr}}}{N_{\mathrm{launch}}}, \tag{9}$$

$$\mathrm{SE}(T) = \sqrt{\frac{T(1-T)}{N_{\mathrm{launch}}}}, \tag{10}$$

Table 1: Material-level extrema from the 96-condition baseline campaign.

Material	Max T	Max mean E (eV)	Min mean E (eV)
Ag	0.8361	13	2.8
Al	0.6536	17.83	15.49
Cu	0.7975	15.55	4.27
Ge	0.8128	16.13	3.903
Si	0.6684	21.48	17.44
Te	0.8452	13.52	2.817

and the arithmetic mean arrival energy is

$$\langle E_{\mathrm{arr}} \rangle = \frac{1}{N_{\mathrm{arr}}} \sum_{i=1}^{N_{\mathrm{arr}}} E_{\mathrm{arr},i}. \tag{11}$$

Arrival-energy summaries include the arithmetic mean, median, 10th and 90th percentiles, and the fractions above 10 and 20 eV. The arithmetic mean is defined by Eq. (11) and is retained to characterize the energetic tail, whereas the median is emphasized as a robust central statistic when the arrival distribution is strongly skewed. An empirical collisionality coordinate is defined as

$$\Pi = PL, \tag{12}$$

where P is the pressure and L is the target–substrate distance. Π is used only as an empirical organizing variable; because $\sigma(E)$ varies with energy, it is not an exact optical depth. This distinction is important when comparing the present results with classical pressure-dependent transport descriptions [2,5,6,8].

3 Results and discussion

3.1 Coupled reduction of transmission and energetic survival

The baseline campaign shows a systematic shift from weakly collisional to strongly collisional transport as pressure and distance increase (Figs. 1–4). At 0.3 Pa and 8 cm, transmission ranges from 0.654 for Al to 0.845 for Te, whereas at 1.0 Pa and 20 cm it ranges from 0.043 for Al to 0.449 for Te (Fig. 2). At the same two endpoints, the mean number of collisions per launched atom rises from approximately 0.94–1.18 to 3.15–10.26, depending on species (Fig. 4). The material-level extrema are summarized in Table 1. The species dependence reflects the role of the projectile/argon mass ratio in both source kinematics and momentum transfer, consistent with established Monte Carlo descriptions of sputtered-atom transport [1,2,6,8].

3.2 Median arrival energy reveals a robust monotonic thermalization trend

For every material, the median arrival energy decreases monotonically with increasing pressure at fixed distance and with increasing distance at fixed pressure (Fig. 5). This response is stronger and more interpretable than the corresponding mean-energy response (Fig. 3) because the mean can remain elevated by a small population of high-energy arrivals. Across the full baseline matrix, the median spans 0.0178–4.9336 eV for Cu, 0.0545–4.5264 eV for Ag, 0.0276–5.3173 eV for Ge, 0.1128–4.7712 eV for Te, 3.7029–6.0585 eV for Al and 4.3425–8.3220 eV for Si. These trends are consistent with the pressure- and distance-dependent thermalization reported in earlier Monte Carlo studies [2,6,8,10,12,15–17].

Linear fits over the investigated window (Table 2) give median-energy slopes between -13.75 and -29.22 eV/(Pa m), with R^2 values from 0.792 to 0.867. Thus, $P{\cdot}L$ is useful as an empirical organizing variable, but the nonidentical slopes demonstrate that the response cannot be collapsed into a single universal, material-independent law.

3.3 Mean–median separation identifies persistent energetic tails

The arrival-energy distributions become increasingly skewed under strongly collisional conditions (Fig. 6 and Table 3). At the condition producing the largest mean/median separation (1.0 Pa and 20 cm), the ratio of mean to median reaches 239.35 for Cu and 141.44 for Ge. Such ratios do not imply that the bulk of arriving atoms retain high energies; rather, they show that a sparse energetic tail can dominate the arithmetic mean. For this reason, the median is used as the principal central-energy metric in the present paper. The distinction between bulk thermalization and energetic tails is also central to previous sputtered-particle transport studies [2,5,6,8,10].

3.4 Angular and radial transport observables

Collisions modify not only energy but also direction. The computed mean incident polar angle (Fig. 7) and radial arrival statistics provide direct transport-level measures of this redistribution. These observables should be interpreted as characteristics of the arriving flux, not as direct predictions of film morphology. The angular response complements the energy and transmission results by showing that increased collisionality redistributes trajectories as well as thermalizing them, in agreement with the role of angular distributions emphasized in earlier Monte Carlo work [3,10,11,15,18].

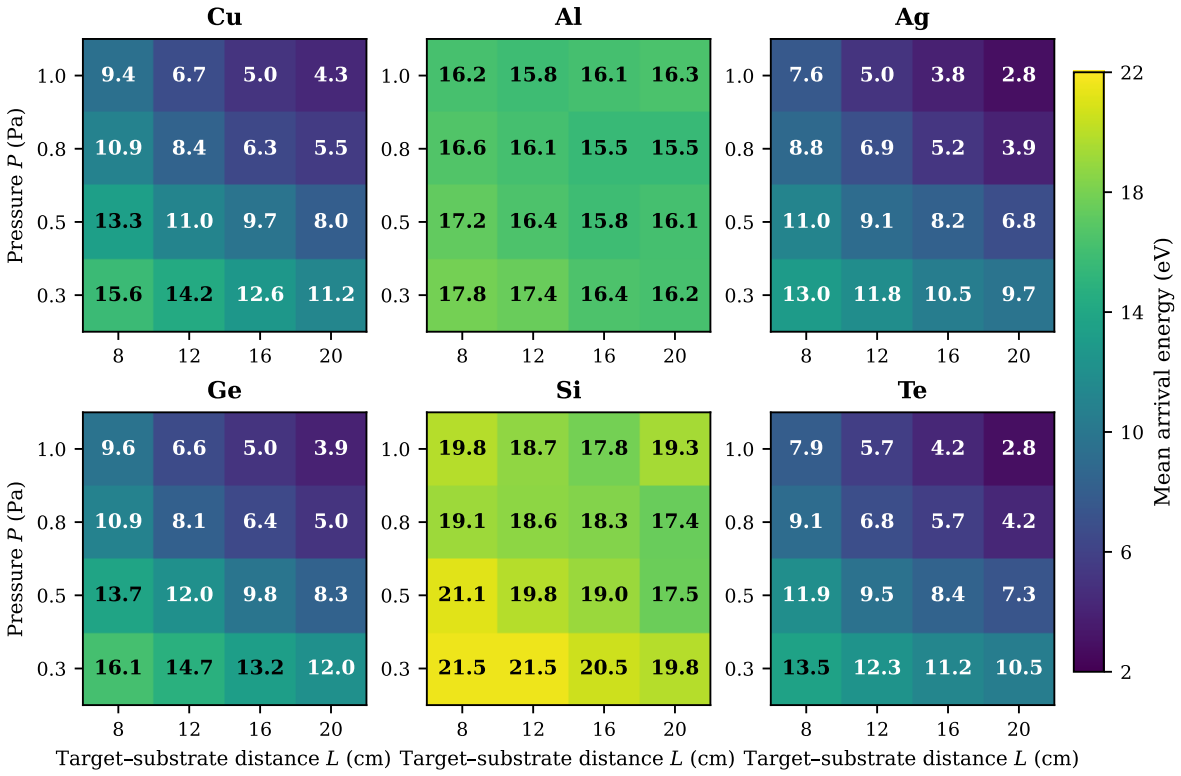

Fig. 1: Mean arrival energy (eV) across the pressure–distance design space for Cu, Al, Ag, Ge, Si and Te. Each cell gives the value for one of the 96 baseline conditions; all panels share the same colour scale.

Table 2: Material-dependent median-energy response to $P{\cdot}L$.

Material	Slope (eV/(Pa m))	Intercept (eV)	R^2	Min median E (eV)	Max median E (eV)
Ag	−24.41	3.926	0.8362	0.05448	4.526
Al	−13.75	5.926	0.858	3.703	6.059
Cu	−26.86	4.149	0.7921	0.01784	4.934
Ge	−29.22	4.548	0.8019	0.02759	5.317
Si	−22.19	8.165	0.8639	4.342	8.322
Te	−26.35	4.416	0.8669	0.1128	4.771

Table 3: Energy-tail amplification measured by the mean/median ratio. P and L give the condition at which the maximum ratio occurs.

Material	Mean/median	Min ratio	Max ratio	P (Pa)	L (cm)
Ag	10.21	2.871	51.39	1.0	20
Al	3.562	2.943	4.414	1.0	20
Cu	27.91	3.152	239.3	1.0	20
Ge	19.36	3.033	141.4	1.0	20
Si	3.23	2.581	4.44	1.0	20
Te	6.743	2.833	24.96	1.0	20

4 Robustness and model sensitivity

4.1 Independent random-seed reproducibility

A separate campaign uses three independent seeds and 10,000 trajectories per seed for all 96 baseline conditions, giving 288 additional simulations. Across the condition matrix, the standard deviation among the three replicate estimates has a median of 0.00374 for transmission, 0.275 eV for mean arrival energy and 0.0736 eV for median arrival energy (Fig. 8 and Table 4). The small replicate-to-replicate dispersion relative to the process trends supports the conclusion that the principal pressure and distance responses are not artefacts of a single random realization. Reproducibility of Monte Carlo

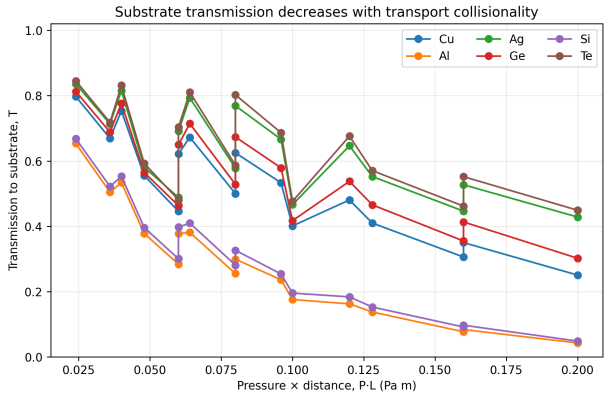

Fig. 2: Substrate transmission versus the empirical collisionality coordinate $P{\cdot}L$.

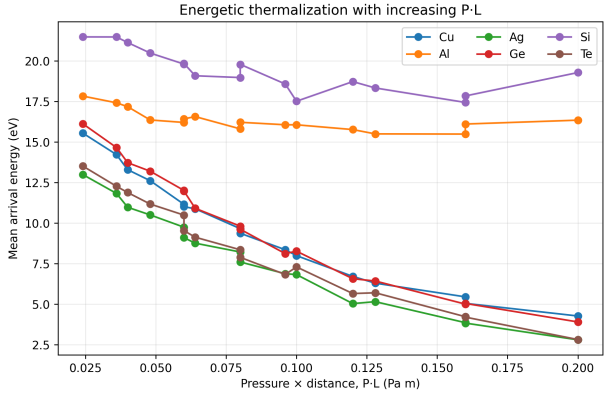

Fig. 3: Mean arrival energy versus $P{\cdot}L$; the arithmetic mean retains information about the high-energy tail.

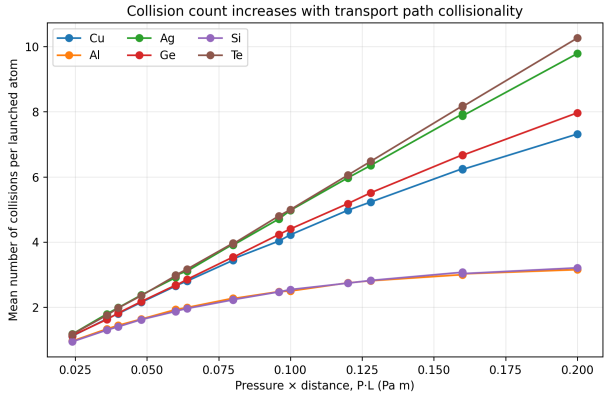

Fig. 4: Mean number of collisions per launched atom versus $P{\cdot}L$.

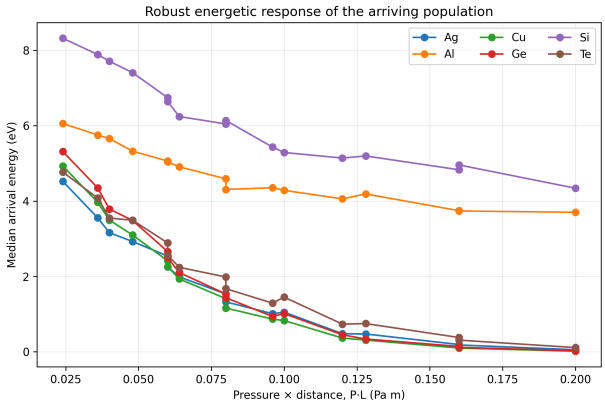

Fig. 5: Median arrival energy versus $P{\cdot}L$. The median decreases monotonically with both pressure and distance for all six materials.

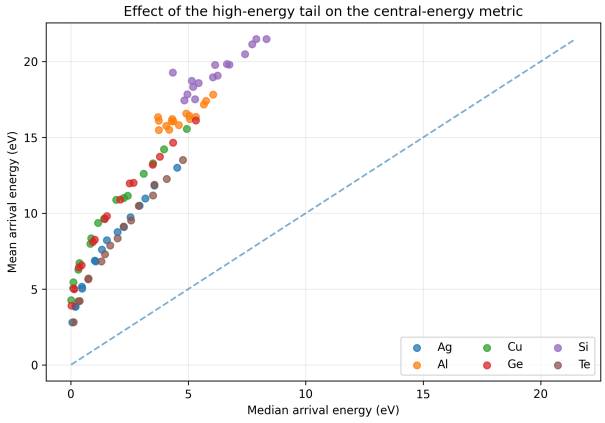

Fig. 6: Mean versus median arrival energy, illustrating the growing influence of a high-energy tail.

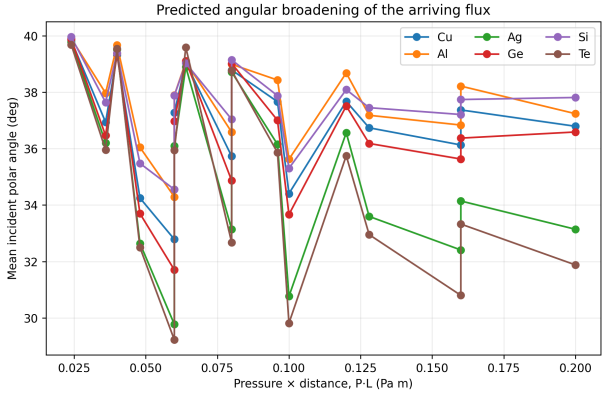

Fig. 7: Mean incident polar angle versus $P{\cdot}L$.

transport calculations is particularly important when the

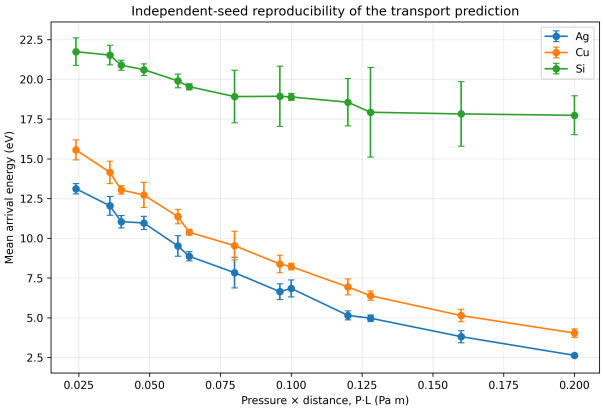

Fig. 8: Independent-seed reproducibility across the baseline condition matrix.

Table 4: Independent-seed reproducibility summary.

Observable	Median SD across 3 seeds
Transmission	0.00374
Mean arrival energy	0.275 eV
Median arrival energy	0.0736 eV

model is used for comparative rather than absolute prediction [2, 6, 9].

4.2 Effective cross-section sensitivity

Because the adopted $\sigma(E)$ is an effective transport model rather than a directly measured microscopic cross section for every target/Ar pair, a dedicated sensitivity campaign was performed. The campaign covers $\sigma_0 = 0.5$, 1.0 and 2.0×10^{-19} m^2 and $\alpha = 0$, 0.18 and 0.36 over selected pressure–distance combinations and all six materials, for 486 additional simulations (Fig. 9 and Table 5). Changing these parameters alters absolute transmission and energy values, as expected, but the central physical interpretation is unchanged: increasing collisional exposure lowers transmission, increases collision counts and shifts the bulk arrival distribution toward lower energy. This sensitivity boundary is consistent with the need to distinguish model-form effects from robust transport trends in Monte Carlo sputtering studies [2, 6–8].

5 Discussion

That higher pressure or a longer target–substrate distance causes energy loss is well established in the sputtered-particle transport literature. What the present campaign adds is a quantitative picture of the coupled response across six species: collisional exposure changes

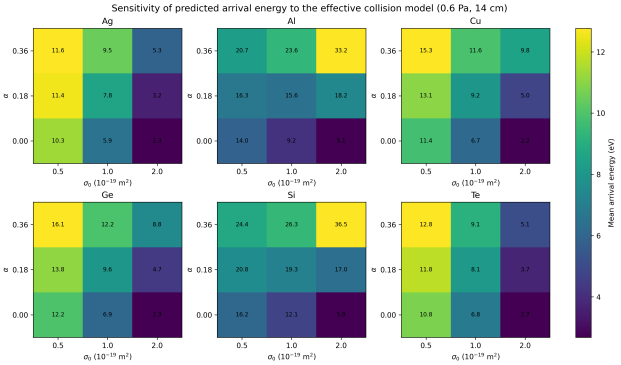

Fig. 9: Sensitivity of selected transport observables to the effective cross-section parameters.

Table 5: Cross-section sensitivity summary: mean arrival energy $\bar{E}$ (eV) at the three levels of each parameter. Levels are $\sigma_0 = 0.5$, 1.0, 2.0×10^{-19} m^2 and $\alpha = 0$, 0.18, 0.36.

Material	Parameter	Level 1	Level 2	Level 3
Ag	σ_0	11.46	8.137	4.656
	α	6.919	8.087	9.249
Al	σ_0	17.39	17.21	19.31
	α	9.96	17.19	26.76
Cu	σ_0	13.41	9.894	6.44
	α	7.567	9.64	12.54
Ge	σ_0	13.97	10.16	6.39
	α	8.063	9.941	12.52
Si	σ_0	20.99	19.96	20.05
	α	12.3	19.23	29.47
Te	σ_0	11.71	8.589	4.821
	α	7.341	8.36	9.423

transmission, collision count, energy percentiles, tail weight and angular properties simultaneously [2–6, 8, 10].

The coordinate $\Pi = P \cdot L$ is useful because both pressure and distance increase the expected opportunity for gas-phase interactions. However, the energy-dependent mean free path prevents Π from being an exact optical-depth variable. Consequently, the observed material-specific slopes are physically meaningful descriptors of the present model window rather than universal constants [2, 6, 8].

A second finding is methodological. Mean arrival energy alone can be misleading when the distribution contains a long energetic tail. The very large mean/median ratios obtained for Cu and Ge at high collisionality demonstrate that a small subset of energetic trajectories can substantially raise the mean after the bulk of the distribution has shifted to sub-eV energies. Transport studies should therefore report at least a robust central statistic and distribution-width information in addition to the mean [2, 5, 6].

The sensitivity study defines the principal boundary of the present work. The effective $\sigma(E)$ model is sufficiently explicit to support reproducible relative comparisons and mechanism-resolved trend analysis, but absolute predictions depend on σ_0 and α. A next-stage model could replace the effective hard-sphere description with species-specific screened-potential scattering or a coupled MC–MD collision treatment, followed by comparison with independently measured deposition profiles or energy-resolved diagnostics [4, 7, 8].

6 Scope and limitations

The simulations reported here predict gas-phase transport observables only; they do not directly predict film thickness, morphology, roughness, crystallinity or composition, aspects addressed separately in the author's earlier work [16–19]. The energy-dependent cross section of Eq. (7) is an effective modelling assumption rather than a measured microscopic cross section for every sputtered-species/Ar pair, which is why the absolute values reported above must be read together with the sensitivity analysis of Section 4.2. In the baseline collision model, the thermal motion of the background gas is not sampled as an independent velocity distribution, and the cosine source law is an explicit approximation; more detailed correlations between the energy and angular distributions of the sputtered source could be incorporated in future work. Finally, no direct experimental validation of the absolute values in the new dataset is claimed: the reproducibility and sensitivity tests establish the internal computational robustness of the results, not their independent experimental validation.

7 Conclusions

A reproducible six-material Monte Carlo campaign generated 1.92 million baseline trajectories over 96 pressure–distance conditions. Transmission decreases and collision counts increase as transport collisionality rises, with quantitatively different responses among Cu, Al, Ag, Ge, Si and Te.

Median arrival energy decreases monotonically with pressure and target–substrate distance for all six materials and is a more robust descriptor than the mean under strongly skewed arrival-energy distributions. $P \cdot L$ is a useful empirical collisionality coordinate over the investigated range, with material-specific median-energy slopes of -13.75 to -29.22 eV/(Pa m) and $R^2 = 0.792$–0.867.

Independent-seed calculations confirm stochastic reproducibility, while cross-section sensitivity tests show that the qualitative trends are robust but absolute values remain model dependent. The main contribution of this work is therefore a coupled, reproducible characterization of transmission, collisions, energy statistics and angular transport, together with explicit statements of uncertainty and model-form boundaries.

References

[1] P. Sigmund, Theory of sputtering. I. Sputtering yield of amorphous and polycrystalline targets, Phys. Rev. **184**, 383–416 (1969). https://doi.org/10.1103/PhysRev.184.383

[2] S. Mahieu, G. Buyle, D. Depla, S. Heirwegh, P. Ghekiere, R. De Gryse, Monte Carlo simulation of the transport of atoms in DC magnetron sputtering, Nucl. Instrum. Methods Phys. Res. B **243**, 313–319 (2006). https://doi.org/10.1016/j.nimb.2005.09.018

[3] D. Depla, W.P. Leroy, Magnetron sputter deposition as visualized by Monte Carlo modeling, Thin Solid Films **520**, 6337–6354 (2012). https://doi.org/10.1016/j.tsf.2012.06.032

[4] G. Zhu, Q. Du, B. Xiao, G. Chen, Z. Gan, Influence of target–substrate distance on the transport process of sputtered atoms: MC–MD multiscale coupling simulation, Materials **15**, 8904 (2022). https://doi.org/10.3390/ma15248904

[5] T. Motohiro, Y. Taga, Monte Carlo simulation of thermalization process of sputtered particles, Surf. Sci. **134**, L494–L499 (1983). https://doi.org/10.1016/0039-6028(83)90304-7

[6] Y. Yamamura, M. Ishida, Monte Carlo simulation of the thermalization of sputtered atoms and reflected atoms in the magnetron sputtering discharge, J. Vac. Sci. Technol. A **13**, 101–112 (1995). https://doi.org/10.1116/1.579874

[7] A.A. Abrahamson, Born–Mayer-type interatomic potential for neutral ground-state atoms with $Z = 2$ to $Z = 105$, Phys. Rev. **178**, 76–79 (1969). https://doi.org/10.1103/PhysRev.178.76

[8] T. Motohiro, Computer simulation, Chapter 4 in: K. Wasa, I. Kanno, H. Kotera (Eds.), Handbook of Sputter Deposition Technology, 2nd ed., William Andrew, Oxford, pp. 143–294 (2012).

[9] A. Bouazza, A. Settaouti, Study and simulation of the sputtering process of material layers in plasma, Monte Carlo Methods Appl. **22**, 149–159 (2016). https://doi.org/10.1515/mcma-2016-0106

[10] A. Bouazza, A. Settaouti, Understanding the contribution of energy and angular distribution in the morphology of thin films using Monte Carlo simulation, Monte Carlo Methods Appl. **24**, 215–224 (2018). https://doi.org/10.1515/mcma-2018-0019

[11] S.E.C. Refas, A. Bouazza, Y. Belhadji, 3D sputtering simulations of the CZTS, Si and CIGS thin films using Monte-Carlo method, Monte Carlo Methods Appl. **27**, 373–382 (2021). https://doi.org/10.1515/mcma-2021-2094

[12] A. Bouazza, Investigation using Monte-Carlo codes simulations for the impact of temperatures and high pressures on thin films quality, Rev. Mex. Fís. **69**, 021501 (2023). https://doi.org/10.31349/RevMexFis.69.021501

[13] A. Bouazza, Revealing the role of vacuum chamber parameters on the pathways leading to substrate deposition by ejected atoms, Int. J. Thin Film Sci. Technol. **12**, 159–162 (2023). https://doi.org/10.18576/ijtfst/120301

[14] M. Koulali, A. Bouazza, An in-depth analysis of investigating and simulating thin film materials using the sputtering process in plasma environments, Int. J. Thin Film Sci. Technol. **14**, 119–124 (2025). https://doi.org/10.18576/ijtfst/140207
[15] A. Bouazza, M.-E. Tchanolo, Modeling pressure and distance effects on particle transport in PVD sputtering using a 3D Monte Carlo approach, Int. J. Thin Film Sci. Technol. **15**, 75–81 (2026). https://doi.org/10.18576/ijtfst/150106
[16] A. Bouazza, Characterizing the relationship between sputtered atom flux generated by electrical discharge in plasma and thin film deposition quality, Int. J. Thin Film Sci. Technol. **13**, 95–100 (2024). https://doi.org/10.18576/ijtfst/130202
[17] A. Bouazza, Computational modeling of magnetron sputtering for thin-film materials: optimizing deposition and analyzing morphology, Bull. Lebedev Phys. Inst. **51**, 324–333 (2024). https://doi.org/10.3103/S1068335624600694
[18] A. Bouazza, 3D visualization of the effect of plasma temperature on thin-film morphology, Bull. Lebedev Phys. Inst. **50**, 7–13 (2023). https://doi.org/10.3103/S1068335623010037
[19] A. Bouazza, Optimization of the cathodic sputtering process for fabricating thin film materials used in modern photovoltaic applications, Int. J. Thin Film Sci. Technol. **13**, 101–105 (2024). https://doi.org/10.18576/ijtfst/130203